?????????????????

ABSTRACT

Paleomagnetism is the main tool used in paleogeographic reconstructions, in which directional information of the past magnetic field is retrieved from ferromagnetic grains (l.s). Magnetic minerals have a wide range of size and composition that influence their magnetic properties and, consequently, their ability to record the directions of paleomagnetic fields. The signals obtained with classical paleomagnetic methodologies are vector averages that include all magnetic grains present in the samples, including the stable and unstable carriers. To improve the quality of the magnetic signal, it would be necessary to individually identify the magnetizations of the carriers of remanent magnetization, in order to isolate only the good registers of the geomagnetic field. This would allow obtaining more reliable paleomagnetic information, as well as possibly being effective for the paleomagnetic study of older rocks (e.g., Archean rocks), meteorites and even bodies with complex geological evolution. Therefore, this project aims to apply magnetic microscopy to identify the remanent magnetization directions of stable magnetic grains and, subsequently, invert these data in an attempt to recover the individual paleomagnetic directions of the magnetic carriers present in the thin-sections. If successful, a new precision methodology for paleomagnetic data acquisition will be implemented.

Keywords: Paleomagnetism, magnetic microscopy, Euler deconvolution, inversion of magnetic data.

INTRODUCTION

Paleomagnetism is the study of the record of the Earth's magnetic field preserved in rocks, being the main tool, and the only quantitative method, used during paleogeographic reconstruction (*Butler*, 1992). It is based on three basic assumptions: (i) the geomagnetic field can be approximated to the field created by a geocentric axial dipole (GAD) aligned with the Earth's axis of rotation over a period that eliminates paleosecular variation ($> 10^4$ years) (*McElhinny and McFadden*, 2000); (ii) ferromagnetic minerals (l.s.) acquire natural remanent magnetization (NRM) parallel to the Earth's geomagnetic field (*Dunlop and Özdemir*, 1997; *Tauxe et al.*, 2018); and (iii) this acquired magnetization is recorded for a long period of time, depending on the physicochemical characteristics of the magnetized mineral, following Neél's Theory (*Néel*, 1949, 1955) and being also influenced by the geological processes by which the rocks were submitted.

The thermoremanent magnetizations (TRMs) of magnetic particles in geological materials are the main records of the direction of the geomagnetic field of the past (*de Groot et al.*, 2014). Iron oxides, such as magnetite, which is the most common magnetic mineral present in rocks (*O'Reilly*, 1984) and acquire TRM as they cool below their Curie temperature and subsequently this direction of magnetization is "frozen" upon reaching blocking temperature (*Dunlop and Özdemir*, 1997). When the grains are small enough, and the magnetization is unidirectional homogeneous (single domain - SD), the acquisition and preservation of magnetic signals is physically supported by Néel's theory (*Néel*, 1949, 1955), conserving the remanent magnetization for long periods of time, on the order of billions of years, and for this reason, they are considered "good recorders" of the paleomagnetic field. In addition to SD, pseudo-single domain (PSD) particles, in the flower and stable vortex states, can also preserve magnetization for periods on the order of the solar system age (*Nagy et al.*, 2017). On the other hand, Néel's theory does not cover larger particles (multi domain - MD), which have unstable remanent magnetization (e.g., caused by viscous reordering of magnetic domains, *de Groot et al.* (2014)), so they are particles with limited ability to record the geomagnetic field. In addition to the magnetic domain state, particles can still vary in composition, size and shape which causes changes in their magnetic properties. All these factors are crucial in determining stable remanence directions used in the calculation of paleomagnetic poles.

Classic techniques for obtaining paleomagnetic data, e.g., thermal demagnetization and alternating fields, are based on the progressive acquisition of the magnetization contained in cylindrical samples, usually of 10 cm^3. The magnetic signal of a single specimen is the result of the sum of moments contained in the assembly of ferromagnetic grains, including stable and unstable registers (*de Groot et al.*, 2021). Although there are recent well-structured studies of imaging magnetic

minerals in thin-sections (e.g., *Almeida et al.*, 2014; *Farchi et al.*, 2017; *Glenn et al.*, 2017; *Lima et al.*, 2014; *Lima and Weiss*, 2009; *Nichols et al.*, 2016; *Weiss et al.*, 2007; *de Groot et al.*, 2018, 2021), obtaining NRM directions of individual grains in the rock fabric remains, to the best of our knowledge, a challenge deeply explored only by *de Groot et al.* (2021). With the possibility of isolating the individual contributions of a fairly large number ($10^6 > N > 10^7$) of stable magnetic particles (SD/PSD) the magnetic directions recovered, using the average of their NRM vectors, would have an accurate paleomagnetic response (*Berndt et al.*, 2016), however such number of observations is unfeasible for the currently insufficient measurements scales of the equipaments (*de Groot et al.*, 2018).

Several branches of Earth Sciences have demonstrated the importance of the "spatiality" of data on a microscopic scale, mainly in Geochemistry and Geochronology, where it is possible to perform punctual analyzes and compositional maps, which allowed significant advances in the understanding of igneous, metamorphic and sedimentary processes (e.g., *Barnes et al.*, 2019; *Davidson et al.*, 2007; *Verberne et al.*, 2020). In Paleomagnetism there has been an interest in point magnetic analyses, or microscale magnetic maps, from magnetic microscopy techniques (*de Groot et al.*, 2014, 2018; *Lima et al.*, 2014; *Weiss et al.*, 2007). However, despite recent advances in this area, still there is no well-established inversion protocol to determine the magnetic vector direction of each individual ferromagnetic grains, nor the intensity of magnetization, without using additional information of the positioning and shape of these sources, such as micromagnetic tomography (e.g., *de Groot et al.*, 2018, 2021; *Fabian and De Groot*, 2019), which is a measurement spatially even more limited than the magnetic microscopy itself.

This paper aims to give a new perspective in the methodological routine that carry out paleomagnetic studies in microscale allowing to retrieve the individual remanent magnetization direction of these stable magnetic carriers (SD and PSD), semi automatically and without any additional information. In this way, a larger area of the thin section can be scanned with the objective of increasing the number of observations and, therefore, increasing the reliability of the directional data obtained. We also intend to generate a micromagnetic analysis protocol in an open source software, based on the techniques that will be described below.

METHODOLOGY

Scanning Magnetic Microscopy

Scanning magnetic microscopy (SMM) is the imaging technique in which a thin-section sample of geological material is horizontally displaced under a high-precision (fixed) micromagnetometer to obtain magnetization (*Weiss et al.*, 2007). The SMM performed at a fixed height above the sample also has the advantage of facilitating the subtraction of the ambient field (constant), to which it might be subject during the scan (*Lima et al.*, 2013). The availability of high-performance and low-cost magnetic sensors has promoted a great advance in the application of SMM in recent years. However, its sensitivity is still a few orders of magnitude lower than that of superconducting quantum interference devices (SQUIDs), the latter being between 10^{-12} and 10^{-15} Am^2 (*Lima et al.*, 2013). This disadvantage is offset by (i) the high spatial resolution of the SMM, as it is performed at a few tens of micrometers from the sampled surface; and (ii) SQUID magnetic microscopy is performed at low temperatures (< 100K), which can cause changes in the original NRM of the sample, while SMM is performed at room temperature (*Lima et al.*, 2013; *Weiss et al.*, 2007).

The SMM can also be considered as a form of aeromagnetic survey, carried out at microscales on sources of flat topography, with high spatial resolution and greater sensitivity to magnetic moment (*Lima et al.*, 2013). An emerging magnetic imaging technology is the quantum diamond microscope (QDM) with very high spatial resolution ($\cong 1$ µm), and can recover magnetic moments as weak as 10^{-17} Am^2, through magnetic sensors located at altitudes between 1 and 5 μm relative to the sample surface capable of detecting the magnetic signals of SD magnetite particles (*Fu et al.*, 2020). Another promising type of magnetic microscope is the magnetic tunnel junction (MTJ) with a spatial resolution greater than 7 μm, a magnetic moment sensitivity of up to 10^{-14} Am^2 and sample-sensor distance of 7 μm. Its advantages reside in the fact that these MTJ devices do not require high bias current to operate (few tens of μA), which avoids induced magnetization signals created by artificial magnetic field during the measurements (*Lima et al.*, 2014).

Due to the similarities between magnetic microscopy techniques and aeromagnetic surveys, the methodologies of data inversion of the latter, densely studied in the last decades, can be adapted for magnetic microscopy. However, *Lima et al.* (2013) report important distinctions between SMM and aeromagnetic surveys, namely: (i) the source distribution in the SMM can often be accurately modeled in a two-dimensional model; (ii) the SMM measures the field produced directly by the sample's NRM; (iii) the sensor positioning is very accurate in the SMM, and the

vertical component of the magnetic field is usually measured, rather than the total field; (iv) there is no need for correction to bring all measurements to the same surface or to grid the data; and (v) the distributions of the magnetization sources are finite and known.

Euler Deconvolution

Thompson (1982) proposed the Euler Deconvolution technique, which is a consolidated method classically applied to data from aeromagnetic surveys that uses first order x, y and z derivatives to determine the positioning and depth of ideal targets (e.g., sphere, cylinder), each characterized by a structural index (*Nabighian et al.*, 2005). Euler deconvolution is one of the most useful methods for estimating the three-dimensional positioning of magnetic sources/geological bodies (*Reid et al.*, 1990). Given the similarities between SMM and aeromagnetic data, its application becomes plausible for determining the positions of magnetic sources caused by ferromagnetic minerals (l.s).

The classic Euler approach is basically the application of a mobile operator in a small data window over the sampled dataset. The observations made within this window are used to estimate the horizontal and vertical positions of the source by solving a small linear system of equations using the gradients of the potential field, provided that the shapes of the sources are assumed. Despite this, this methodology usually yields a large number of solutions (*Barbosa and Silva*, 2011), which becomes a limitation for the method. In an attempt to circumvent the problem of this expressive cloud of solutions, we suggest a previous application of a method for delimitating the region of each source that generates the potential field and later the application of Euler's Deconvolution. Hence giving a single system of linear equations to be solved for each source.

Derivative-based filters are widely used to emphisize the potencial anomaly signal of shallower sources and applied in modern methods for edge/position detection, as of the solution of Euler equation itself requires the gradient of the potential field. Since the calculation of first order derivatives is a must in this case, we might as well give preference to filtering techniques that use the same products. One good filtering example is the so called horizontal gradient method (∇H, Equation (1)) (*Cordell and Grauch*, 1982), which is a source edge detection methodology where the response of a target's horizontal gradient tends to overlap its own limits, thus obtaining a two-dimensional robust map of the sources location *Blakely* (1996). Another popular method for locating edges of magnetic bodies is the total gradient (∇T, Equation (2)), which places the source's maximum anomaly values over the area inside its boundaries, despite of geomagnetic latitude, magnetization direction or source dip/geometry (*Nabighian et al.*, 2005). Both total and horizontal

gradients are reliable techniques to be applied with the SMM data.

$$\nabla H = \sqrt{\left(\frac{\partial F}{\partial x}\right)^2 + \left(\frac{\partial F}{\partial y}\right)^2} \qquad (1)$$

$$\nabla T = \sqrt{\left(\frac{\partial F}{\partial x}\right)^2 + \left(\frac{\partial F}{\partial y}\right)^2 + \left(\frac{\partial F}{\partial z}\right)^2} \qquad (2)$$

After pre processing the data with derivative-based filter, highlighting the sources edges, it is possible to apply blob detection techniques. The latter refers to visual algorithms and/or modules with the ability of detecting points/regions that are either darker or brighter than the neighborhood. The most common and accurate approach to detect brighter blobs on dark surroundings is the Laplacian of Gaussian (LoG), its downside is also being slower than other approaches (*Han and Uyyanonvara*, 2016; *Kong et al.*, 2013). We used the scikit-image blob detection python library (*van der Walt et al.*, 2014) to identify the window region of data that embraces each isolated source by applying the algorithm on the highlighted sources map (∇T or ∇H). Therefore, the blobs selected are local maxima obtained with successively LoG images. Once the target location window is determined, subsequently, the Euler Deconvolution can applied in this single static data window yeilding only one solution per source. Thus, being an automatic, faster and easier way than the classical methodology of solving the Euler equation.

Euler Deconvolution Formulation

The anomaly of a potential field F produced by a three-dimensional source, whose cartesian coordinates of its central position are x_c, y_c and z_c, satisfies the homogeneous Euler equation (*Reid et al.*, 1990) expressed by:

$$(x - x_c) \cdot \frac{\partial F}{\partial x} + (y - y_c) \cdot \frac{\partial F}{\partial y} + (z - z_c) \cdot \frac{\partial F}{\partial z} = n \cdot (b - F) \qquad (3)$$

where: n is the structural index, that is, a gauge of the geometric shape of the sources causing the anomaly; and b is the constant, and unknown, base level.

The Euler's Deconvolution uses the gradient of a potential field and the structural index, which can be defined by the geometric nature of the sources. The structural index is the only necessary a priori knowledge. Once a value for n is assumed

($n = 3$ for spherical/punctual magnetic sources), the homogeneous Euler equation can be rearranged as follows:

$$x_c \cdot \frac{\partial F}{\partial x} + y_c \cdot \frac{\partial F}{\partial y} + z_c \cdot \frac{\partial F}{\partial z} + n \cdot b = x \cdot \frac{\partial F}{\partial x} + y \cdot \frac{\partial F}{\partial y} + z \cdot \frac{\partial F}{\partial z} + n \cdot F \qquad (4)$$

The Equation (4) can be written in matrix form as:

$$\begin{bmatrix} Fx_1 & Fy_1 & Fz_1 & n \\ Fx_2 & Fy_2 & Fz_2 & n \\ \vdots & \vdots & \vdots & \vdots \\ Fx_N & Fy_N & Fz_N & n \end{bmatrix} \begin{bmatrix} x_c \\ y_c \\ z_c \\ b \end{bmatrix} = \begin{bmatrix} x_1 \cdot Fx_1 + y_1 \cdot Fy_1 + z_1 \cdot Fz_1 + n \cdot F_1 \\ x_2 \cdot Fx_2 + y_2 \cdot Fy_2 + z_2 \cdot Fz_2 + n \cdot F_2 \\ \vdots \\ x_N \cdot Fx_N + y_N \cdot Fy_N + z_N \cdot Fz_N + n \cdot F_N \end{bmatrix} \qquad (5)$$

Where: Fx_i, Fy_i and Fz_i represent, respectively, the gradients $\frac{\partial F}{\partial x}$, $\frac{\partial F}{\partial y}$ and $\frac{\partial F}{\partial z}$ evaluated on the i-th observation point ($i = 1, 2, ..., N$). While x_i, y_i and z_i represent the cartesian coordinates at the i-th observation point.

Note that Equation (5) is a linear system $\bar{\bar{G}} \cdot \bar{p} = \bar{d}$ and its objective function $f(\bar{p})$ expressed by:

$$f(\bar{p}) = \|e\|^2 = (\bar{\bar{G}} \cdot \bar{p} - \bar{d})^T \cdot (\bar{\bar{G}} \cdot \bar{p} - \bar{d}) \qquad (6)$$

The solution $\bar{p}$ of the system can be obtained by minimizing the objective function ($\frac{\partial f}{\partial p_k} = \bar{0}$) through the least squares estimator given by:

$$\bar{p} = \left(\bar{\bar{G}}^T \cdot \bar{\bar{G}} \right)^{-1} \cdot \left(\bar{\bar{G}}^T \cdot \bar{d} \right) \qquad (7)$$

Thus, $\bar{p} = [x_c \ y_c \ z_c \ b]^T$ will be the solution vector that satisfies Euler's Equation with the least possible error containing the position coordinates source center (x_c, y_c, z_c) and the base level (b).

Magnetic Inversion

The rapid inversion of the total field is a method developed by *Oliveira Jr. et al.* (2015) being computationally efficient to invert the magnetic anomalies produced

by multiple sources with approximately spherical shapes to estimate their magnetization directions (inclination and declination). This methodology requires the central position of the magnetic sources, which can be obtained with Euler Deconvolution, and the information on their geometry helps to reduce the non-exclusivity of the problem. In this way, it is possible to estimate the direction of magnetization from multiple sources. The method does not require that all sources have the same magnetization direction nor the use of regularly spaced data on a horizontal grid, and can still be implemented in linear and non-linear inversion problems.

Currently, the main inversion limitations for these type of data are: (i) in part because the sampling scale during measurement is insufficiently accurate and (ii) because of the non-singularity of the magnetic inversion (*Lima et al.*, 2013). The basic mathematical structure associated with the inverse problem of aeromagnetic data can be adapted and used in SMM data due to its similarity, despite the non-singularity caused by the infinite number of solutions for the same observed magnetic field (*Weiss et al.*, 2007). Assigning as much information as possible about the analyzed sample and the experimental environment can reduce this ambiguity by recovering the magnetization direction. In particles with unidirectional magnetization, and without magnetization sources outside the sample area, it is possible to guarantee singularity for the inverse problem in SMM (*Baratchart et al.*, 2013). Associating the fact that there is a singularity in the response of uniformly magnetized particles and that ferromagnetic particles (*l.s.*) with stable magnetization have such a characteristic, therefore, the inversion method becomes ideal for the purpose of this project.

Parametrization and Forward Model

Let $\bar{B}$ be the observed data vector, whose i-th element $\bar{B}_i$, $i = 1, 2, ..., N$, is a total field anomaly, resulting from the NRM contribution of each ferromagnetic particle (*l.s.*), measured at position (x_i, y_i, z_i) (black dots, Figure 1a). In this cartesian coordinate system, x points to geographic north, y points east, and z points down. In general, the magnetic field that is produced in the thin section is the result solely and exclusively of the NRM contribution of the particles without considering the induced component, since the measurements carried out in the magnetic microscope are usually made under magnetic shielding conditions. Thereby, approximating the shape of ferromagnetic minerals (*l.s.*) to NRM magnetizing spheric/punctual sources. According to *Blakely* (1996) the equation of a uniformly magnetized sphere is given by:

$$b = C_m \cdot \frac{4}{3} \cdot \pi \cdot R^3 \cdot M \cdot \hat{M} \cdot \frac{1}{r^2} \cdot \hat{r} \tag{8}$$

Whereas the magnetic sources can be represented by a set of L uniformly magnetized spheres. In this case, each sphere will have a contribution in the field measured at the position (x_i, y_i, z_i):

$$b_i^j = C_m \cdot \frac{4}{3}\pi \cdot R_j^3 \cdot \bar{M}^j \cdot \frac{1}{r_{i,j}^2} \cdot \hat{r}_{i,j} , \quad j = 1, 2 \ldots, L \tag{9}$$

Where: $C_m = \frac{\mu_0}{4\pi} = 10^{-7} \frac{H}{m}$; R_j is the radius of the j-th sphere; $r_{i,j}$ is the distance (unit vector $\hat{r}_{i,j}$) between the center of the j-th sphere and the observation point i, i = 1, 2, . .. N; and $\bar{M}^j = \begin{bmatrix} Mx_j & My_j & Mz_j \end{bmatrix}^T$ is the vector formed by the cartesian components of the magnetization of the j-th sphere (unit vector $\hat{M}^j$).
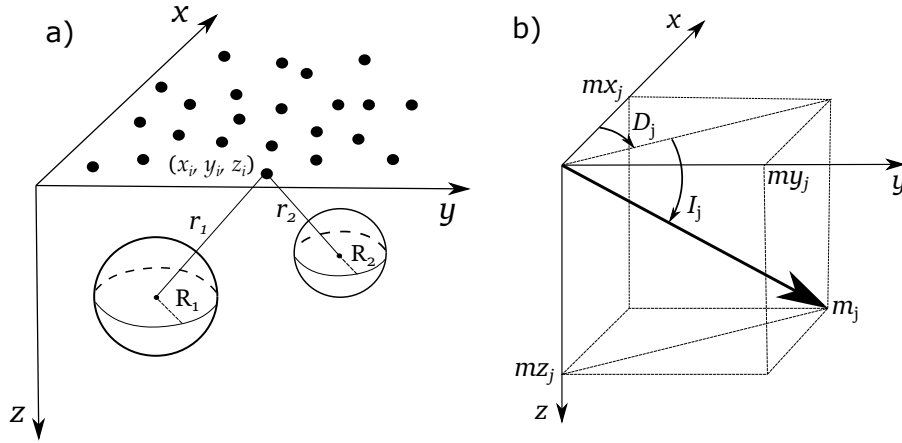
Figure 1: a) Schematic representation of spheres (L = 2) uniformly magnetized in the subsurface, whose magnetic effect can be observed at points (x_i, y_i, z_i), i = 1, 2, ..., N (black dots). In this cartesian coordinate system x, y and z corresponds to geographic north, east and z, respectively. b) Schematic cartesian representation of vector m_j with elements mx_j, my_j and mz_j, with declination D_j (positive clockwise) and inclination I_j (positive downwards), j = 1, 2, ... L. Modified from: *Oliveira Jr. et al.* (2015).

Thus, the total magnetization measured at the position (x_i, y_i, z_i) will be the sum of contributions from the L spheres, given by:

$$B_i = \sum_{j=1}^{L} b_i^j \tag{10}$$

The Equation (9) presents the sensitive matrix A_i^j and the m_j, which is the vector

that encompasses the cartesian components of the magnetc moment (magnetization times volume) of each sphere:

$$A_i^j = C_m \cdot \left[\begin{array}{ccc} \left(\frac{\partial^2}{\partial x \partial x} \cdot \frac{1}{r_{i,j}}\right) & \left(\frac{\partial^2}{\partial x \partial y} \cdot \frac{1}{r_{i,j}}\right) & \left(\frac{\partial^2}{\partial x \partial z} \cdot \frac{1}{r_{i,j}}\right) \\ \left(\frac{\partial^2}{\partial x \partial y} \cdot \frac{1}{r_{i,j}}\right) & \left(\frac{\partial^2}{\partial y \partial y} \cdot \frac{1}{r_{i,j}}\right) & \left(\frac{\partial^2}{\partial x \partial z} \cdot \frac{1}{r_{i,j}}\right) \\ \left(\frac{\partial^2}{\partial x \partial z} \cdot \frac{1}{r_{i,j}}\right) & \left(\frac{\partial^2}{\partial y \partial z} \cdot \frac{1}{r_{i,j}}\right) & \left(\frac{\partial^2}{\partial z \partial z} \cdot \frac{1}{r_{i,j}}\right) \end{array} \right]_{3N \times 3L} , m_j = \begin{bmatrix} Mx_j \cdot \frac{4}{3}\pi \cdot R_j^3 \\ My_j \cdot \frac{4}{3}\pi \cdot R_j^3 \\ Mz_j \cdot \frac{4}{3}\pi \cdot R_j^3 \end{bmatrix}_{3L \times 1} \quad (11)$$

$$\text{Where: } \frac{1}{r_j} \equiv \frac{1}{\sqrt{\left(x_i - xc_j\right)^2 + \left(y_i - yc_j\right)^2 + \left(z_i - zc_j\right)^2}}$$

Subsequently, the components of the total magnetizing field can be obtained (from Equation (10)), as shown below:

$$C_m \cdot \left[\begin{array}{ccc} \left(\frac{\partial^2}{\partial x \partial x} \cdot \frac{1}{r_{i,j}}\right) & \left(\frac{\partial^2}{\partial x \partial y} \cdot \frac{1}{r_{i,j}}\right) & \left(\frac{\partial^2}{\partial x \partial z} \cdot \frac{1}{r_{i,j}}\right) \\ \left(\frac{\partial^2}{\partial x \partial y} \cdot \frac{1}{r_{i,j}}\right) & \left(\frac{\partial^2}{\partial y \partial y} \cdot \frac{1}{r_{i,j}}\right) & \left(\frac{\partial^2}{\partial x \partial z} \cdot \frac{1}{r_{i,j}}\right) \\ \left(\frac{\partial^2}{\partial x \partial z} \cdot \frac{1}{r_{i,j}}\right) & \left(\frac{\partial^2}{\partial y \partial z} \cdot \frac{1}{r_{i,j}}\right) & \left(\frac{\partial^2}{\partial z \partial z} \cdot \frac{1}{r_{i,j}}\right) \end{array} \right]_{3N \times 3L} \cdot \begin{bmatrix} Mx_j \cdot \frac{4}{3}\pi \cdot R_j^3 \\ My_j \cdot \frac{4}{3}\pi \cdot R_j^3 \\ Mz_j \cdot \frac{4}{3}\pi \cdot R_j^3 \end{bmatrix}_{3L \times 1} = \begin{bmatrix} Bx_i \\ By_i \\ Bz_i \end{bmatrix}_{3N \times 1}$$

$$(12)$$

As in the specific case in the study of magnetic microscopy, in the routine practice, the vertical component of magnetization is usually measured. In this case, there is a need to adapt the Equation (12) to isolate the response from the vertical component (B_z). Therefore, the equation of the direct model will be given by:

$$C_m \cdot \left[\left(\frac{\partial^2}{\partial x \partial z} \cdot \frac{1}{r_{i,j}}\right) \quad \left(\frac{\partial^2}{\partial y \partial z} \cdot \frac{1}{r_{i,j}}\right) \quad \left(\frac{\partial^2}{\partial z \partial z} \cdot \frac{1}{r_{i,j}}\right) \right]_{N \times 3L} \cdot \begin{bmatrix} Mx_j \cdot \frac{4}{3}\pi \cdot R_j^3 \\ My_j \cdot \frac{4}{3}\pi \cdot R_j^3 \\ Mz_j \cdot \frac{4}{3}\pi \cdot R_j^3 \end{bmatrix}_{3L \times 1} = [Bz_i]_{N \times 1} \quad (13)$$

The magnetization is usually represented in spherical coordinates of intensity (M (A/m)), declination (D (°)) and inclination (I (°)). Thus, the vector $\bar{M}_j$, containing the cartesian coordinates of magnetization, of the direct model can also be calculated as follows:

$$\begin{bmatrix} Mx_j \\ My_j \\ Mz_j \end{bmatrix}_{3L \times 1} = M_j \cdot \begin{bmatrix} cos\left(I_j\right) \cdot cos\left(D_j\right) \\ cos\left(I_j\right) \cdot sin\left(D_j\right) \\ sin\left(I_j\right) \end{bmatrix}_{3L \times 1} \quad (14)$$

10

We can simplify the Equation (13) to:

$$C_m \cdot \left[\left(\frac{\partial^2}{\partial x \partial z} \cdot \frac{1}{r_{i,j}} \right) \quad \left(\frac{\partial^2}{\partial y \partial z} \cdot \frac{1}{r_{i,j}} \right) \quad \left(\frac{\partial^2}{\partial z \partial z} \cdot \frac{1}{r_{i,j}} \right) \right]_{N \times 3L} \cdot \begin{bmatrix} mx_j \\ my_j \\ mz_j \end{bmatrix}_{3L \times 1} = [Bz_i]_{N \times 1} \qquad (15)$$

With this, the Equation (15) can be rewritten in linear form, given by:

$$\bar{\bar{A}} \cdot \bar{m} = \bar{B}_z \qquad (16)$$

Inverse Model

Assuming that the ferromagnetic minerals (*l.s.*) that give rise to the observed magnetization component data vector $\bar{B}_z$ can be approximated by a set of L uniformly magnetized spheres with known coordinates (xc_j, yc_j, zc_j), j = 1, 2, ..., L, of their centers. Also assuming that there is no induced magnetization component, only that of the NRM. Under these assumptions, a superdetermined inverse linear problem is formulated to estimate the vector of parameters $\bar{m}$ (Equation (16)) from the observed data $\bar{B}_z$ and $\bar{\bar{A}}$, the latter being obtained previously with the Euler Deconvolution.

The problem of estimating a parameter vector $\bar{m}$ containing the spheres' magnetic moment vectors can be solved by minimizing the objective function $f(\bar{m})$:

$$f(\bar{m}) = \|e\|^2 = e^T \cdot e = (\bar{\bar{A}} \cdot \bar{m} - \bar{d})^T \cdot (\bar{\bar{A}} \cdot \bar{m} - \bar{B}_z) \qquad (17)$$

When differentiating the (Equation (17)) by $\bar{m}$ and equating the result to the zero vector ($\frac{\partial f}{\partial m_k} = \bar{0}$). Then we obtain the normal equation for estimating least squares solution given by:

$$\bar{m} = \left(\bar{\bar{A}}^T \cdot \bar{\bar{A}} \right)^{-1} \cdot \left(\bar{\bar{A}}^T \cdot \bar{B}_z \right) \qquad (18)$$

The least squares estimator is also known to be affected by outliers in the data set (*Aster et al.*, 2019). Since the environment of an SMM acquisition is very well controlled, the probability of occurrence of ouliers is considerably low. With that, in case there is an exception to the rule, we also implement a robust estimator to remove the influence of outliers (Also adapted from: *Oliveira Jr. et al.*, 2015). This formulation is detailed in the Appendix A.1.

Directions of Magnetization and Uncertainty Propagation

In paleomagnetic studies the magnetization vectors are represented in terms of their declination (D) and inclination (I). These are given as a function of the magnetization vector $\bar{m}_j$ (Equation (15)) and represented in spherical coordinates (as shown in Figure 1b).

In this way, it is possible to determine the directions (D_j and I_j) and magnetic moment (m_j) for the j-th sphere of the set of L spheres by using:

$$D_j = \tan^{-1}\left(\frac{my_j}{mx_j}\right) \tag{19}$$

$$I_j = \tan^{-1}\left(\frac{mz_j}{\sqrt{(mx_j)^2 + (my_j)^2}}\right) \tag{20}$$

$$m_j = \sqrt{(mx_j)^2 + (my_j)^2 + (mz_j)^2} \tag{21}$$

In a micromagnetic survey, or any geophysical survey, measurements are affected by noise caused by experimental errors and equipment inaccuracies. Noise in the observed data vector $\bar{B}_z$ affects the solution of the estimated parameter vector $\bar{m}_j$, regardless of the method used. Assuming that the noise during the measurement of the observed data is independent and with variance σ_0^2, one can quantify this effect on the estimated parameters through propagation of the covariance (*Aster et al.*, 2019). The covariance matrix of these parameters will be given by:

$$\bar{\bar{Cov}}\left(\bar{m}_j\right) = \sigma_0^2 \cdot \left(\bar{\bar{A}}^T \cdot \bar{\bar{A}}\right)^{-1} \quad \text{(least square)} \tag{22}$$

The main diagonal of the covariance matrix (Equation (22) contains the variance of each member of the parameter vector, as expressed below:

$$\bar{\bar{Cov}} = \left[\ diag\left(\sigma_{mx_1}^2 \quad \sigma_{my_1}^2 \quad \sigma_{mz_1}^2 \quad \cdots \quad \sigma_{mz_L}^2\right)\right]_{3L \times 3L} \tag{23}$$

Thus, for the j-th sphere:

$$\sigma_{mx_j} = \sqrt{\sigma_{mx_j}^2}, \quad \sigma_{my_j} = \sqrt{\sigma_{my_j}^2} \quad \text{and} \quad \sigma_{mz_j} = \sqrt{\sigma_{mz_j}^2} \tag{24}$$

Thus, the propagation of uncertainties of the declination (D_j), inclination (I_j) and magnetic moment (m_j) results are given as a function of the parameters (detailed in Appendix A.2) obtained in Equation (24):

$$\sigma_{D_j} = \sqrt{\left(\frac{\partial D_j}{\partial mx_j}\right)^2 \cdot \left(\sigma_{mx_j}\right)^2 + \left(\frac{\partial D_j}{\partial my_j}\right)^2 \cdot \left(\sigma_{my_j}\right)^2} \tag{25}$$

$$\sigma_{I_j} = \sqrt{\left(\frac{\partial I_j}{\partial mx_j}\right)^2 \cdot \left(\sigma_{mx_j}\right)^2 + \left(\frac{\partial I_j}{\partial my_j}\right)^2 \cdot \left(\sigma_{my_j}\right)^2 + \left(\frac{\partial I_j}{\partial mz_j}\right)^2 \cdot \left(\sigma_{mz_j}\right)^2} \tag{26}$$

$$\sigma_{m_j} = \sqrt{\left(\frac{\partial m_j}{\partial mx_j}\right)^2 \cdot \left(\sigma_{mx_j}\right)^2 + \left(\frac{\partial m_j}{\partial my_j}\right)^2 \cdot \left(\sigma_{my_j}\right)^2 + \left(\frac{\partial m_j}{\partial mz_j}\right)^2 \cdot \left(\sigma_{mz_j}\right)^2} \tag{27}$$

APLICATION TO SYNTHETIC DATA

In order to test the efficiency of the proposed inversion method, we applied it to two sets of synthetic data contaminated by high and/or low frequency noise.

The first synthetic test is performed by generating a simple set of four spheres with similar magnetization intensity and radius, but completely different magnetization directions. Generating a data set contaminated by high frequency noise. In this simulation, the magnetization directions and magnetic moment intensity are directly compared with the initial input parameters. This first simplified test is basically done to investigate the efficiency of the inversions used for Euler positioning and magnetization parameters, thus being a validation of the methodology.

The second data set is data generated by a more complex model containing one hundred spheres with different radius and magnetization intensity, but magnetized in a similar direction within one standard deviation. This data set is corrupted by both low and high frequency noise. In this second application there is also validation using the comparison of the model data with the retrieved data. The complexity of this synthetic data seeks to more faithfully simulate the applicability of the proposed method to real SMM data.

Simple Simulation: Validating the Methodology

We applied the proposed method in a numerical simulation of a geological thin-section of dimensions 1000 µm x 1000 µm in a regular grid (1000 x 1000) for estimating the magnetization directions of four spherical sources uniformly magnetized (but with different directions), according to Table 1. Totaling an observation number $N = 10^6$ obtained at a sensor-sample distance of 5 µm and a grid spacing of 1 µm. Subsequently, the data vector was contaminated with a pseudo-random noise of normal Gaussian distribution with a zero mean and 15 nT standard deviation, as shown in Figure 2a.

Table 1: Each source positioning and magnetization parameters modelled and recovered using least square estimator, respectively.

Sphere	Center coordinates			Magnetization		
	Xc (μm)	Yc (μm)	Zc (μm)	m ($A \cdot m^2$)	D (°)	I (°)
1	250.00	250.00	5.30	8.70e-15	-140.00	-30.00
	250.03	249.94	5.37	8.80e-15 $\pm$ 1.39e-17	-140.22 $\pm$ 0.11	-30.04 $\pm$ 0.08
2	500.00	500.00	7.75	7.63e-15	-70.00	-50.00
	499.96	500.00	7.76	7.65e-15 $\pm$ 1.89e-17	-69.42 $\pm$ 0.26	-49.85 $\pm$ 0.15
3	750.00	750.00	8.50	6.21e-15	10.00	62.00
	749.98	749.97	8.56	6.29e-15 $\pm$ 1.98e-17	9.06 $\pm$ 0.50	62.34 $\pm$ 0.22
4	200.00	800.00	10.00	4.97e-15	125.00	22.00
	200.10	800.12	9.99	4.92e-15 $\pm$ 3.00e-17	124.63 $\pm$ 0.39	21.76 $\pm$ 0.27

The first step is to apply the upward continuaton filter, which transforms the potencial field measured on a surface into one measured at a higher surface level (*Blakely*, 1996), therefore smoothing out high frequency noise. This first step is always needed in high frequency noisy data, since the Euler equation requires the first derivatives of potencial field. If this step is negleted or badly elaborated, the high frequency noise propagation during the application of the derivative filters will cause future errors in the next methodological stage.

The next step is to calculate the magnetic total gradient (or horizontal gradient) filter in order to highlight the anomaly signal of each source within its own boundaries, then we apply the blob detection algorithm (*van der Walt et al.*, 2014) to obtain a robust positioning of each source data window (Figure 2b).

After isolating the potencial field data and first derivatives for each source, we can solve the 3D Euler deconvolution Equation (4) proposed by *Reid et al.* (1990), one for each subarea selected (window data), by assuming the structural index of a sphere/punctual source ($n = 3$). Thus, obtaining a sturdy result for the central positioning (Xc, Yc, Zc) of each source causing the magnetic potential anomaly in the observed data set, as shown in Table 1.
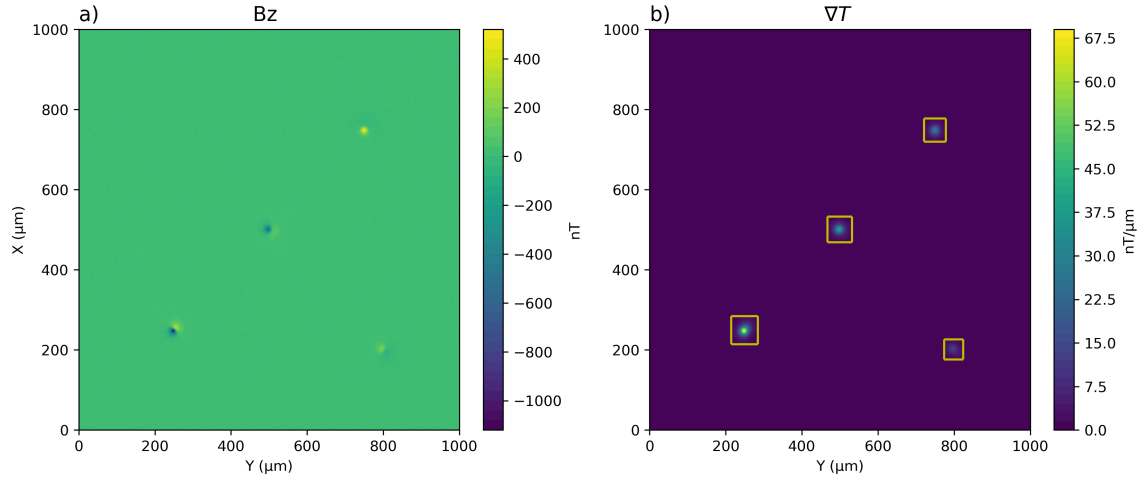
Figure 2: a) Synthetic data contaminated with psedo-random normal noise. b) Individual sources window position (yellow squares) obtained with the blob detection algorithm applied on the total gradient map.

The last step consists of using the central positions of each source, obtained with Euler's method, as an input parameter for inverting the original noisy data (Figure 2a) to find the least squares (or robust) approximation solution for the vector of cartesian magnetic moments ($\bar{m}$). With this, the magnetization directions (D and I) and the intensity of the magnetic moment can be estimated using equations (Equations (19) to (21)), as well as the uncertainty propagation of this inversion, using equations (Equations (25) to (27)) and considering σ = 25nT. The results obtained with the least squares estimator can also be seen in Table 1.

It is important to emphasize that *Oliveira Jr. et al.* (2015) proved that the magnetization directions (D and I) recovered by the least squares estimator is sensitive to variations in the horizontal coordinates (x and y) of the magnetic sources central positions. While, the same being practically insensitive to variations in depths. Thus, the same authors consider Euler deconvolution method as an adequate technique to estimate the central positions that will be used as a priori information for inversion. This occurs mainly because, when well performed, the recovery of the horizontal coordinates of sources central position is considerably accurate, while the vertical coordinate can undergo greater variation (*Silva and Barbosa*, 2003; *Melo et al.*, 2013), even so the inversion will still provide extremely satisfactory results. The high sensitivity of Euler deconvolution to high frequency noise can also be easily overcome with the proper application of the upward continuation filter.

15

Complex Simulation: Testing Applicability

This test tries to replicate a more complicated scenario by simulating a hundred sources randomly distributed in the imaged area of the synthetic thin section of 2000 x 1400 μm, with 2 μm grid spacing and 5 μm sample-sensor distance. For greater fidelity with real samples, the magnetic sources have different diameters, magnetizations and depths. The depths of the spheres vary between 1 and 19 μm, while the radii have values that range from 0.01 to 0.95 μm. The magnetization acquisition simulates an induced field with both declination and inclination directions of 45°. However, as seen in real data, these directions have both varying declination and inclination, but averaging centered in the direction of the induced field. Therefore, both the NRM declination and inclination of the particles were selected using pseudo-random normal distribution with mean 45°and standard deviation of 8°. Finally, high (pseudo-random normal with zero mean and standard deviation of 5 nT) and low frequency noises were added to the anomaly data of the vertical field component of the magnetic field, which can be seen in Figure 3a.

After applying the same filtering steps described earlier on the simple synthetic sample, the blob detection algorithm was applied on the total gradient anomaly map and the individual source windows were selected (Figure 3b). The latter was able to detect 84 magnetic particles. The solution of Euler's equation was then determined for each data window to later be used as input data for inversion of magnetic moments.
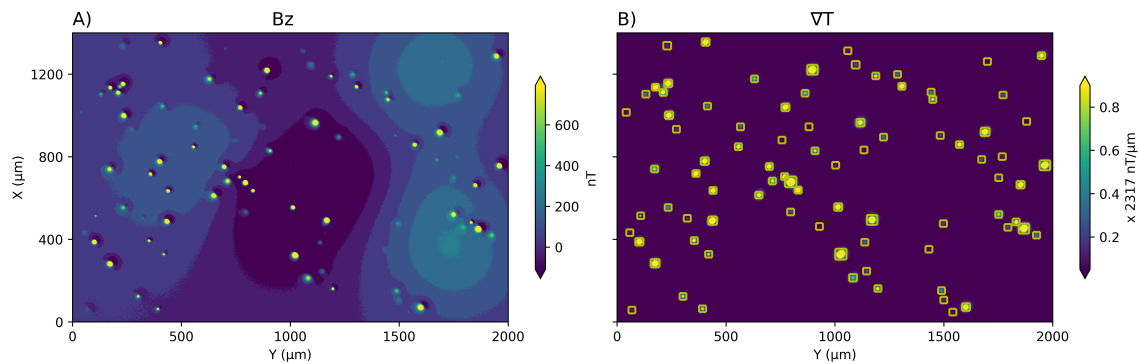
Figure 3: a) Complex synthetic data contaminated with both high and low frequencies noise. b) Individual sources window position (yellow squares) obtained with the blob detection algorithm applied on the total gradient map.

The spatiality of the inversion results is one of the great differences between the application of magnetic microscopy and the classic techniques of paleomagnetism. Thus, the validation of these results is expressed individually in the windows

obtained with the blob detection through the declination, inclination and magnetic moment misfits (Figure 4a-c, respectively), in addition to the determination coefficient R^2 obtained by comparing the forward model and the observed data (Figure 4d). As both the depth and the size of the particles influence the magnetic signal generated by them, this information is also given in these graphs in the form of a cross bar. Where the vertical bars scale with the depth of the sources (max = 19 μm), while the horizontal bars scale with the radius (max = 0.95 μm).
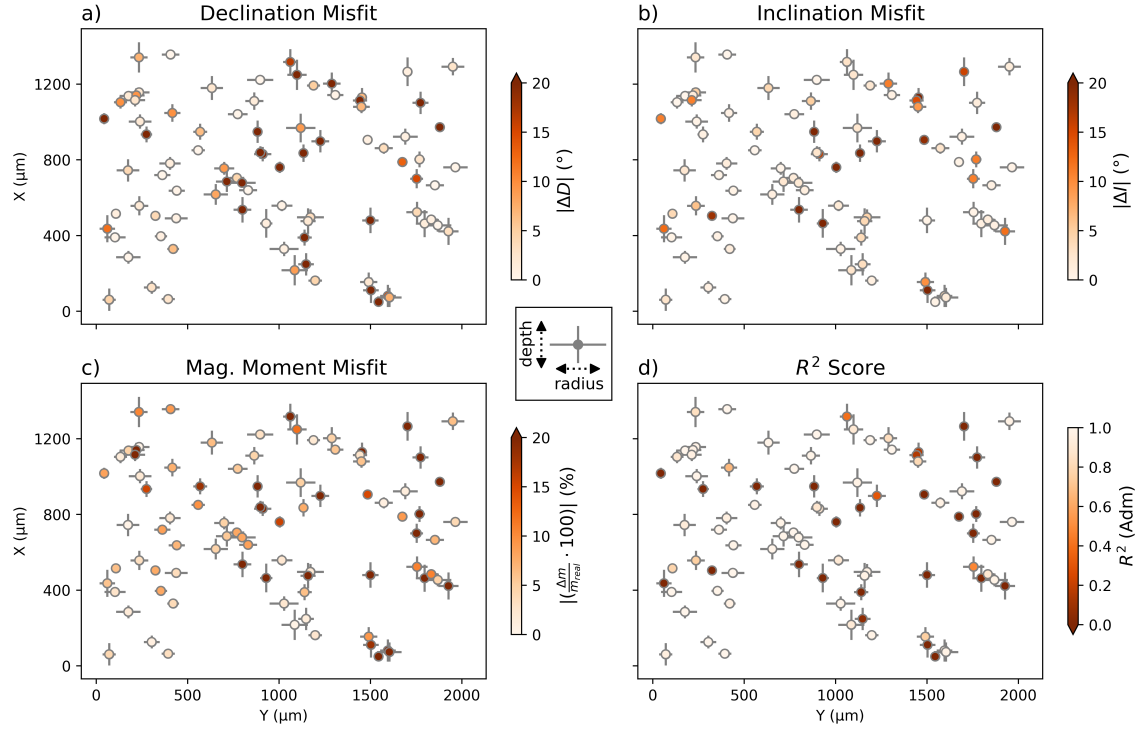
Figure 4: The validation of the result obtained with the inversion was calculated for each individual particle based on the error between the real parameters modeled and their respective recovered values, being directions of (a) declination and (b) inclination and (c) intensity of magnetic moment , in addition to the R^2 score (d) obtained by comparing the forward model and the actual data. The depth and radius of the magnetic sources are also important factors that influence the final result, therefore, these data are given in the form of cross plots, with the vertical bar represented by the depth (1 - 19 μm) and the horizontal bar by the radius (0.01 - 0.95 μm).

The application in complex synthetic data also allows observing the strengths and limitations of the proposed methodology. Some of the strengths that can be mentioned are: (i) the fact that the applied technique not only detects most of the modeled sources, but also (ii) most of the recovered magnetic parameters have considerably low errors, especially in the declination and inclination directions, usually less than 5°(Figure 4a-b). (iii) The magnetic moments obtained also tend

to not deviate much from the real values (Figure 4c) when the R^2 scores are high (Figure 4d). (iv) Shallow particles grouped in clusters are usually well individualized during window selection, as well as (v) some weak signal but isolated particles.

While, the limitations observed were already expected, namely (i) the blob detection is insensitive when there are sources that are very close, grouping them in the same window, thus causing an erroneous result both for Euler deconvolution and for the magnetic parameters. (ii) The very same occurs when there is a source under another, in this case the magnetic signal is a sum of both. (iii) In clusters of larger and/or deeper particles, although the method individualizes them well, the magnetic signal of the neighboring particles can considerably influence the result of the inversion

Apparently there is a direct relationship between the vertical position and depth with the observed errors. It is clear from cross bars on the Figure 4 that deep particles and/or with small radii generate worse results than those more superficial particles with larger radii, this is mainly because these two properties will influence the signal picked up by the sensor. Small particles have weaker magnetic moment signal, in addition, very deep sources have their signal considerably attenuated at the height of the sensor, when both characteristics are present at the same time the error tends to be greater. The opposite is also true, larger particles and superficial particles have their signal better captured by the sensor. Small and superficial particles might also generate low errors because, despite having lower magnetic moments, the sensor-sample distance is sufficient to generate a good signal.

The modeled magnetization directions not only generate an average direction coincident with the simulated induced field, but also have relatively small Fisher cones of confidence (*Fisher et al.*, 1987) due to their clustering (Figure 5a). On the other hand, the recovered directions may be more sparse, despite this the mean direction obtained is statically the same as the field modeled inside the 95% confidence cone (Figure 5b). If necessary, the data can be filtered according to the highest adjustments obtained with the coefficient of determination (R^2). The value of R^2 can vary from $-\infty$ to 1, with values closest to 1 corresponding to the best modeling results. Thus, filtering the results obtained with the magnetic inversion with $R^2 \geq 0.7$ we obtain the directions closest to the average and less sparse, maintaining the high reliability result (Figure 5c).
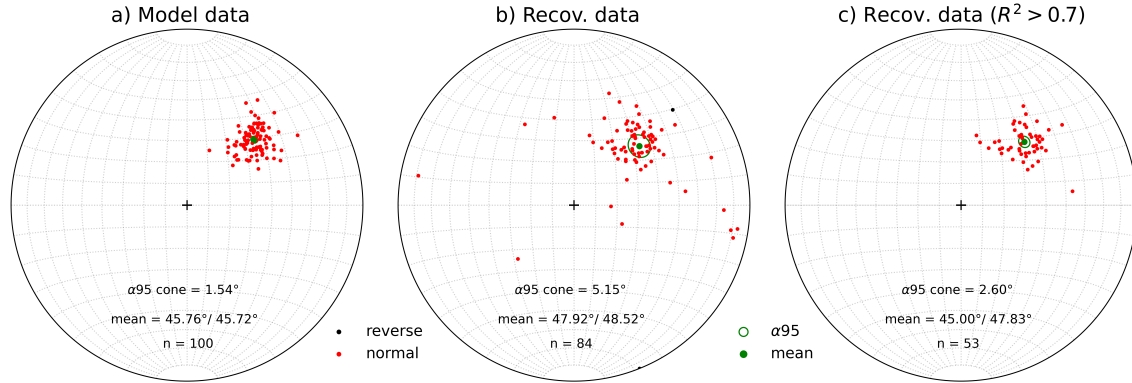
Figure 5: a) The real data models a thin section of rock with particles uniformly magnetized in the average direction of the induced field 45°/45°. b) The recovered data, without any type of filtering, are sparse, but statistically generate the same average direction. c) It is still possible to filter only the directions of the magnetic sources with the best fitting determined by the coefficient of determination (e.g., $R^2 \geq 0.7$) to ensure better grouping of the directions around the mean value.

APLICATION TO REAL DATA

DISCUSSION

CONCLUSION

We developed an efficient semi-automated method to determine the direction of magnetization of dipolar sources on a microscale, as well as the recovery of their magnetic moment. Being ideal for a reinterpretation for the application of methods of paleomagnetic studies using thin sections of rock samples. This would be an attempt to improve the quality of results obtained by isolating the responses of more reliable recorders of the Earth's geomagnetic field.

We also present a new, faster and cleaner way to solve the Euler equation in determining the positioning of magnetic anomaly sources using a pre-selection of magnetic anomaly source windows based on the Laplacian of the Gaussian applied to total gradient anomaly maps. In this way, reducing the numerous solutions to just one data window per source. After estimating the structural index ($n = 3$) by approximating the sources generating the magnetic anomaly to

spheres/points, the Euler deconvolution is performed and the central position of each source is determined.

Since for the recovery of direction and magnetization we only need to assume that the sources have their central positions known (so we apply Euler deconvolution) and that their magnetizations are uniform. This last premise aligns with the theory of magnetically stable particles, which are the basis of classical paleomagnetism. Also, there is no need for any kind of prior knowledge other than the observed magnetic anomaly, and the structural index of the sources. Therefore, this method can be quickly replicated in a dataset of thin sections of rocks to obtain the distributions of magnetic directions of each source identified in the sample.

The test using a simply synthetic sample shows the great capability of the method by retrieving not only the precisely center positions

REFERENCES

Almeida, T. P., T. Kasama, A. R. Muxworthy, W. Williams, L. Nagy, and R. E. Dunin-Borkowski, Observing thermomagnetic stability of nonideal magnetite particles: Good paleomagnetic recorders?, *Geophysical Research Letters*, *41*(20), 7041–7047, doi:10.1002/2014GL061432, 2014.

Aster, R. C., B. Borchers, and C. H. Thurber, *Parameter Estimation and Inverse Problems*, Elsevier, San Diego, USA, doi:10.1016/C2015-0-02458-3, 2019.

Baratchart, L., D. P. Hardin, E. A. Lima, E. B. Saff, and B. P. Weiss, Characterizing kernels of operators related to thin-plate magnetizations via generalizations of Hodge decompositions, *Inverse Problems*, *29*(1), 015,004, doi:10.1088/0266-5611/29/1/015004, 2013.

Barbosa, V. C., and J. B. Silva, Reconstruction of geologic bodies in depth associated with a sedimentary basin using gravity and magnetic data, *Geophysical Prospecting*, *59*(6), 1021–1034, doi:10.1111/j.1365-2478.2011.00997.x, 2011.

Barnes, C., J. Majka, D. Schneider, K. Walczak, ·. Michał Bukała, K. Kośmińska, T. Tokarski, and A. Karlsson, High-spatial resolution dating of monazite and zircon reveals the timing of subduction-exhumation of the Vaimok Lens in the Seve Nappe Complex (Scandinavian Caledonides), *Contributions to Mineralogy and Petrology*, *174*, 5, doi:10.1007/s00410-018-1539-1, 2019.

Berndt, T., A. R. Muxworthy, and K. Fabian, Does size matter? Statistical limits of paleomagnetic field reconstruction from small rock specimens, *Journal of Geophysical Research: Solid Earth*, *121*(1), 15–26, doi:10.1002/2015JB012441, 2016.

Blakely, R. J., *Potential Theory in Gravity and Magnetic Applications*, 461 pp., Cambridge University Press, Cambridge, 1996.

Butler, R. F., *Paleomagnetism: magnetic domains to geologic terranes*, 238 pp., Blackwell Scientific Publications, Boston, doi:10.5860/choice.29-5708, 1992.

Cordell, L., and V. I. Grauch, Mapping basement magnetitation zones from aeromagnetic data in the san juan basin, New Mexico, in *1982 SEG Annual Meeting, SEG 1982*, pp. 246–247, Society of Exploration Geophysicists, doi:10.1190/1.0931830346.ch16, 1982.

Davidson, J. P., D. J. Morgan, B. L. Charlier, R. Harlou, and J. M. Hora, Microsampling and isotopic analysis of igneous rocks: Implications for the study of magmatic systems, *Annual Review of Earth and Planetary Sciences*, *35*, 273–311, doi:10.1146/annurev.earth.35.031306.140211, 2007.

de Groot, L. V., K. Fabian, I. A. Bakelaar, and M. J. Dekkers, Magnetic force microscopy reveals meta-stable magnetic domain states that prevent reliable absolute palaeointensity experiments, *Nature Communications*, *5*(1), 1–10, doi:10.1038/ncomms5548, 2014.

de Groot, L. V., K. Fabian, A. Béguin, P. Reith, A. Barnhoorn, and H. Hilgenkamp, Determining Individual Particle Magnetizations in Assemblages of Micrograins, *Geophysical Research Letters*, *45*(7), 2995–3000, doi:10.1002/2017GL076634, 2018.

de Groot, L. V., et al., Micromagnetic Tomography for Paleomagnetism and Rock-Magnetism, *Journal of Geophysical Research: Solid Earth*, *126*(10), e2021JB022,364, doi:10.1029/2021JB022364, 2021.

Dunlop, D. J., and Ö. Özdemir, *Rock Magnetism Fundamentals and Frontiers*, 573 pp., Cambridge University Press, doi:10.1017/cbo9780511612794, 1997.

Fabian, K., and L. V. De Groot, A uniqueness theorem for tomography-assisted potential-field inversion, *Geophysical Journal International*, *216*(2), 760–766, doi:10.1093/GJI/GGY455, 2019.

Farchi, E., Y. Ebert, D. Farfurnik, G. Haim, R. Shaar, and N. Bar-Gill, Quantitative Vectorial Magnetic Imaging of Multi-Domain Rock Forming Minerals Using Nitrogen-Vacancy Centers in Diamond, *SPIN*, *7*(3), 1740,015, doi:10.1142/S201032471740015X, 2017.

Fisher, N. I., T. Lewis, and B. J. J. Embleton, *Statistical Analysis of Spherical Data*, Cambridge University Press, doi:10.1017/CBO9780511623059, 1987.

Fu, R. R., E. A. Lima, M. W. Volk, and R. Trubko, High-Sensitivity Moment Magnetometry With the Quantum Diamond Microscope, *Geochemistry, Geophysics, Geosystems*, *21*(8), e2020GC009,147, doi:10.1029/2020GC009147, 2020.

Glenn, D. R., R. R. Fu, P. Kehayias, D. Le Sage, E. A. Lima, B. P. Weiss, and R. L. Walsworth, Micrometer-scale magnetic imaging of geological samples using a quantum diamond microscope, *Geochemistry, Geophysics, Geosystems*, *18*(8), 3254–3267, doi:10.1002/2017GC006946, 2017.

Han, K. T. M., and B. Uyyanonvara, A Survey of Blob Detection Algorithms for Biomedical Images, in *7th International Conference of Information and Communication Technology for Embedded Systems (IC-ICTES)*, pp. 57–60, IEEE, doi:10.1109/ICTEmSys.2016.7467122, 2016.

Kong, H., H. C. Akakin, and S. E. Sarma, A Generalized Laplacian of Gaussian Filter for Blob Detection and Its Applications, *IEEE Transactions on Cybernetics*, *43*(6), 1719–1733, doi:10.1109/TSMCB.2012.2228639, 2013.

Lima, E. A., and B. P. Weiss, Obtaining vector magnetic field maps from single-component measurements of geological samples, *Journal of Geophysical Research: Solid Earth*, *114*(6), 6102, doi:10.1029/2008JB006006, 2009.

Lima, E. A., B. P. Weiss, L. Baratchart, D. P. Hardin, and E. B. Saff, Fast inversion of magnetic field maps of unidirectional planar geological magnetization, *Journal of Geophysical Research: Solid Earth*, *118*(6), 2723–2752, doi:10.1002/jgrb.50229, 2013.

Lima, E. A., A. C. Bruno, H. R. Carvalho, and B. P. Weiss, Scanning magnetic tunnel junction microscope for high-resolution imaging of remanent magnetization fields, *Measurement Science and Technology*, *25*(10), 105,401, doi:10.1088/0957-0233/25/10/105401, 2014.

McElhinny, M. W., and L. P. McFadden, Rock Magnetism, in *Paleomagnetism*, edited by M. W. McElhinny and L. P. McFadden, pp. 31–77, Academic Press, doi:10.1016/S0074-6142(00)80095-9, 2000.

Melo, F. F., V. C. Barbosa, L. Uieda, V. C. Oliveira, and J. B. Silva, Estimating the nature and the horizontal and vertical positions of 3D magnetic sources using Euler deconvolution, *Geophysics*, *78*(6), J87–J98, doi:10.1190/GEO2012-0515.1, 2013.

Nabighian, M. N., V. J. S. Grauch, R. O. Hansen, T. R. LaFehr, Y. Li, J. W. Peirce, J. D. Phillips, and M. E. Ruder, The historical development of the magnetic method in exploration, *GEOPHYSICS*, *70*(6), 33ND–61ND, doi:10.1190/1.2133784, 2005.

Nagy, L., W. Williams, A. R. Muxworthy, K. Fabian, T. P. Almeida, P. Ó. Conbhuí, and V. P. Shcherbakov, Stability of equidimensional pseudo–single-domain magnetite over billion-year timescales, *Proceedings of the National Academy of Sciences*, *114*(39), 10,356–10,360, doi:10.1073/PNAS.1708344114, 2017.

Néel, L., Theorie du trainage magnetique des ferromagnetiques en grains fins avec applications aux terres cuites, *Ann. Geophys.*, *5*, 99–136, 1949.

Néel, L., Some theoretical aspects of rock-magnetism, *Advances in Physics*, *4*(14), 191–243, doi:10.1080/00018735500101204, 1955.

Nichols, C. I., J. F. Bryson, J. Herrero-Albillos, F. Kronast, F. Nimmo, and R. J. Harrison, Pallasite paleomagnetism: Quiescence of a core dynamo, *Earth and Planetary Science Letters*, *441*, 103–112, doi:10.1016/j.epsl.2016.02.037, 2016.

Oliveira Jr., V. C., D. P. Sales, V. C. Barbosa, and L. Uieda, Estimation of the total magnetization direction of approximately spherical bodies, *Nonlinear Processes in Geophysics*, *22*(2), 215–232, doi:10.5194/npg-22-215-2015, 2015.

O'Reilly, W., Applications of rock and mineral magnetism, in *Rock and Mineral Magnetism*, pp. 194–212, Springer US, doi:10.1007/978-1-4684-8468-7_9, 1984.

Reid, A. B., J. M. Allsop, H. Granser, A. J. Millett, and I. W. Somerton, Magnetic interpretation in three dimensions using Euler deconvolution, *GEOPHYSICS*, *55*(1), 80–91, doi:10.1190/1.1442774, 1990.

Silva, J. B., and V. C. Barbosa, 3D Euler deconvolution: Theoretical basis for automatically selecting good solutions, *Geophysics*, *68*(6), 1962–1968, doi:10.1190/1.1635050, 2003.

Tauxe, L., S. Banerjee, R. F. Butler, and R. Van der Voo, tauxe Essentials of Paleomagnetism: Fifth Web Edition, 2018.

Thompson, D. T., EULDPH: a new technique for making computer-assisted depth estimates from magnetic data., *Geophysics*, *47*(1), 31–37, doi:10.1190/1.1441278, 1982.

van der Walt, S., J. L. Schönberger, J. Nunez-Iglesias, F. Boulogne, J. D. Warner, N. Yager, E. Gouillart, and T. Yu, scikit-image: image processing in Python, *PeerJ*, *2*, e453, doi:10.7717/peerj.453, 2014.

Verberne, R., S. M. Reddy, D. W. Saxey, D. Fougerouse, W. D. Rickard, D. Plavsa, A. Agangi, and A. R. Kylander-Clark, The geochemical and geochronological implications of nanoscale trace-element clusters in rutile, *Geology*, *48*(11), 1126–1130, doi:10.1130/G48017.1, 2020.

Weiss, B. P., E. A. Lima, L. E. Fong, and F. J. Baudenbacher, Paleomagnetic analysis using SQUID microscopy, *Journal of Geophysical Research: Solid Earth*, *112*(9), 9105, doi:10.1029/2007JB004940, 2007.

APPENDIX A

Appendix A.1

As the least squares estimate (Equation (18)) is very sensitive to the presence of outliers in the observed data, the estimated parameters could be seriously misleading. To counteract this problem *Oliveira Jr. et al.* (2015) suggest a robust scheme based on the minimization of the objective function obtained with the absolute error:

$$f\left(\widetilde{m}\right) = \left(\sum_{i=1}^{N} \left| \left(\bar{\bar{A}} \cdot \bar{m} \right)_i - (\bar{B}_z)_i \right| \right) \tag{28}$$

Unlike the solution presented for the objective function in Equation (18), the parameter vector minimizing Equation (28) cannot be obtained as a simple linear system. A practical way is the iteratively reweighted least squares algorithm (*Aster et al.*, 2019; *Oliveira Jr. et al.*, 2015). In this algorithm, at each iteration k, the following linear system is solved:

$$\widetilde{m}^{k+1} = \left(\bar{\bar{A}}^T \cdot \bar{\bar{R}}^k \cdot \bar{\bar{A}} \right)^{-1} \cdot \left(\bar{\bar{A}}^T \cdot \bar{\bar{R}}^k \cdot \bar{B}_z \right) \tag{29}$$

The term $\bar{\bar{R}}^k$ is an N × N diagonal matrix whose i-th element r_i^k (i = 1, 2, ..., N) is given by:

$$r_i^k = \frac{1}{\left| \left(\bar{\bar{A}} \cdot \bar{m} \right)_i - \bar{B}_{zi} + e \right|} \tag{30}$$

Where: e is a small positive number used to prevent singularities

This iterative process starts (k = 0) with the solution vector obtained by the least squares estimator (Equation (18)). From this initial approximation $\widetilde{m}^0$, we calculate the matrix $\bar{\bar{R}}^0$ (Equation (30)). Which is used in the solution of the linear system given by Equation (29) to obtain the estimate $\widetilde{m}^1$. Later using this updated estimate to calculate the new matrix $\bar{\bar{R}}^1$ (Equation (30)), we solve the linear system (Equation (29)) to obtain a new estimate $\widetilde{m}^2$, and so on. As the iterations progress, this iterative procedure tends to converge and estimate $\widetilde{m}$, which is called robust estimate (*Oliveira Jr. et al.*, 2015). According to *Aster et al.* (2019) this convergence can be limited by a tolerance τ, given by:

$$\frac{\|\widetilde{m}^{k+1} - \widetilde{m}^k\|}{1 + \|\widetilde{m}^{k+1}\|} \leq \tau \tag{31}$$

Where: τ is a positive number (*e.g.*, 10^{-2}) chosen by the algorithm user.

The convariance matrix for the uncertainties propagation also is updated with the $\bar{\bar{R}}^k$, as shown in the Equation (32):

$$\overline{Cov}\left(\widetilde{m_j}\right) = {\sigma_0}^2 \cdot \left(\overline{\overline{A}}^T \cdot \overline{\overline{R}}^k \cdot \overline{\overline{A}}\right)^{-1} \quad (robust) \tag{32}$$

Appendix A.2

The derivatives of the propagation functions of the uncertainties of the declination (σ_{D_j}), inclination (σ_{I_j}) and magnetic moment (σ_{m_j}) in relation to each parameter (mx_j, my_j, mz_j) are detailed below:

$$\frac{\partial D_j}{\partial mx_j} = \frac{-my_j}{mx_j{}^2 + my_j{}^2} \tag{33}$$

$$\frac{\partial D_j}{\partial my_j} = \frac{mx_j}{mx_j{}^2 + my_j{}^2} \tag{34}$$

$$\frac{\partial I_j}{\partial mx_j} = \frac{-mx_j \cdot mz_j}{\sqrt{mx_j{}^2 + my_j{}^2} \cdot \left(mx_j{}^2 + my_j{}^2 + mz_j{}^2\right)} \tag{35}$$

$$\frac{\partial I_j}{\partial my_j} = \frac{-my_j \cdot mz_j}{\sqrt{mx_j{}^2 + my_j{}^2} \cdot \left(mx_j{}^2 + my_j{}^2 + mz_j{}^2\right)} \tag{36}$$

$$\frac{\partial I_j}{\partial mz_j} = \frac{\sqrt{mx_j{}^2 + my_j{}^2}}{\left(mx_j{}^2 + my_j{}^2 + mz_j{}^2\right)} \tag{37}$$

$$\frac{\partial m_j}{\partial mx_j} = \frac{mx_j}{\sqrt{mx_j{}^2 + my_j{}^2 + mz_j{}^2}} \tag{38}$$

$$\frac{\partial m_j}{\partial my_j} = \frac{my_j}{\sqrt{mx_j{}^2 + my_j{}^2 + mz_j{}^2}} \tag{39}$$

$$\frac{\partial m_j}{\partial mz_j} = \frac{mz_j}{\sqrt{mx_j{}^2 + my_j{}^2 + mz_j{}^2}} \tag{40}$$